

ARTICLE OPEN



Development of an interfering peptide M1-20 with potent anti-cancer effects by targeting FOXM1

Huitong Bu¹, Xianling Lan¹, Haojie Cheng¹, Chaozhu Pei¹, Min Ouyang¹, Yan Chen¹, Xiaoqin Huang¹, Li Yu¹ and Yongjun Tan¹

© The Author(s) 2023

Disrupting protein–protein interactions (PPIs) has emerged as a promising strategy for cancer drug development. Interfering peptides disrupting PPIs can be rationally designed based on the structures of natural sequences mediating these interactions. Transcription factor FOXM1 overexpresses in multiple cancers and is considered an effective target for cancer therapeutic drug development. Using a rational design approach, we have generated a peptide library from the FOXM1 C-terminal sequence and screened FOXM1-binding peptides. Combining FOXM1 binding and cell inhibitory results, we have obtained a FOXM1-targeting interfering peptide **M1-20** that is optimized from the natural parent peptide to the D-retro-inverso peptide. With improved stability characteristics, **M1-20** inhibits proliferation and migration, and induces apoptosis of cancer cells. Mechanistically, **M1-20** inhibits FOXM1 transcriptional activities by disrupting its interaction between the MuvB complex and the transcriptional co-activator CBP. These are consistent with the results that **M1-20** suppresses cancer progression and metastasis without noticeable toxic and side effects in wild-type mice. These findings reveal that **M1-20** has the potential to be developed as an anti-cancer drug candidate targeting FOXM1.

Cell Death and Disease (2023)14:533; <https://doi.org/10.1038/s41419-023-06056-9>

INTRODUCTION

Transcription factors are associated with the initiation and progression of cancers, and are recognized as potential targets for developing novel cancer therapeutics [1]. Modulating the expression and stability of transcription factors, or interfering with their binding to DNA sequences, can affect their activity [2]. However, disrupting protein–protein interactions (PPIs) is a promising strategy for cancer drug development [3], particularly through the use of interfering peptides that bind to the large, flat contact surfaces mediating PPIs. In practice, interfering peptides that abolish the functions of transcription factors can be predicted by so-called rational design strategies, wherein peptides are produced based on the natural amino acid sequences of PPI surfaces [4]. So far, several interfering peptides targeting transcription factors have been validated for cancer treatment in preclinical studies (e.g., TCF4 N-terminus-derived peptide targeting β -catenin:TCF interaction [5], p73 DBD-derived peptide targeting p53:p73 interaction [6], and GAPDH-derived peptide targeting p53:GAPDH interaction [7]) or in clinical trials (e.g., NSC745104 targeting p53:HDM2 interaction [8] and Omo-103 targeting C-Myc:Max interaction [9]). All these interfering peptides have been rationally designed based on the structures of natural sequences that mediate the PPIs of transcription factors.

FOXM1 is a member of the forkhead box (FOX) transcription factor family [10], and expresses in all developmental embryo tissues but only in adult tissues with a high proliferation index [11]. In multiple cancers, FOXM1 is upregulated and its levels in clinical

cancer samples can predict disease diagnosis and prognosis [12]. FOXM1 stimulates the cell cycle, promoting malignant proliferation through the transcriptional activation of genes involved in G1/S and G2/M transitions [13]. It is also involved in cancer cell metastasis [14], and maintaining the characteristics of cancer stem cells [15]. Additionally, FOXM1 stimulates the expression of DNA damage repair-related genes in cancer cells [16], while inhibition of FOXM1 can enhance the sensitivity of cancers to chemical therapeutics [17]. As a survival protein, FOXM1 specifically protects cancer cells from apoptosis by upregulating antiapoptotic genes [18]. Given its multiple roles in promoting cancer progression, FOXM1 is considered a potential target for cancer therapy development [19]. Several small molecule compounds, including Thiostrepton [20], RCM [21], antibiotic Siomycin A [22], and FDI-6 [23], can impair the growth of cancer cells by disrupting FOXM1 transcriptional activities. A FOXM1 DBD-specific single-strand DNA aptamer has also been selected to inhibit FOXM1 transcriptional functions in cancer cells [24]. Besides, a recombinant protein M1-138 has been generated to target FOXM1 in cancer cells by fusing the FOXM1 N-terminal domain (1-138aa) with a cell-penetrating peptide [25]. Currently, there are no commercially available anti-cancer therapeutics specifically targeting FOXM1.

Two mechanisms by which FOXM1 activates transcription have been established. First, FOXM1 directly binds to its conserved DNA motif of RYAAAYA (FKH motif) in downstream gene promoters, such as CDC25B, through its DNA-binding domain (DBD, 232-332aa) to activate their transcription [26]. Second, FOXM1 can

¹State Key Laboratory of Chemo/Biosensing and Chemometrics, College of Biology, Hunan Engineering Research Center for Anticancer Targeted Protein Pharmaceuticals, Hunan University, Changsha, Hunan 410082, China. email: yjtan@hnu.edu.cn
Edited by Boris Zhivotovsky

Received: 22 April 2023 Revised: 1 August 2023 Accepted: 9 August 2023

Published online: 19 August 2023

stimulate gene expression through an indirect DNA binding mechanism mediated by the MuvB complex [27]. This complex, composed of multiple subunits including LIN9, binds to the CHR (Cell cycle genes Homology Region) motif (TTTGAA or TTATAA) [28] in target gene promoters and controls precisely timed transcription of the cell cycle. LIN9 in the MuvB complex interacts with the FOXM1 N-terminal domain and recruit FOXM1 to the promoters of certain cell cycle genes, like PLK1, enabling its target gene transcription without direct DNA binding [29]. The transcriptional activities of FOXM1 also rely on its C-terminal domain that interacts with the transcription co-activator CBP [30], which is essential for inducing gene transcription through acetylating histone [31] and initiating RNA Pol II basal complex [32]. In addition, the FOXM1 N-terminal domain can interact with other cancer-related transcription factors, such as β -catenin or Smad3, facilitating their nuclear import process to fully activate the classical WNT or TGF- β signaling pathway [33, 34].

In this study, we intend to develop interfering peptides targeting FOXM1 for cancer treatment. The FOXM1 C-terminal domain is an ideal target for screening interfering peptides as it interacts with the N-terminal domain, which mediates PPIs with multiple partner proteins [35]. These peptides may also have the potential to disrupt FOXM1 transcriptional activities by competing with FOXM1:CBP interaction. Based on the rational design strategy, we have developed an interfering peptide (**M1-20**) that potently binds to FOXM1 and inhibits its transcriptional activities by disrupting interactions between the FOXM1 N-terminal domain and the MuvB complex or between FOXM1 and CBP. **M1-20** inhibits cancer cell proliferation and migration and induces apoptosis of cancer cells *in vitro* and *in vivo*, without obvious toxic and side effects, indicating its potential for developing anti-cancer drugs.

MATERIALS AND METHODS

Cell culture

HEK293T, MDA-MB-231, MCF7, ZR-75-30, MCF10A, HeLa, U2OS, A549, and 4T1 cells were obtained from ATCC (Manassas, USA). Details were described in the supplemental materials and methods.

Luciferase reporter assay

The luciferase enzyme activities were measured with the Dual-Luciferase Reporter Assay System (Promega, USA) following the manufacturer's instructions. The detailed protocols were described in the supplemental materials and methods.

Solid-phase synthesis of peptides

Peptides were generated in a solid phase synthesizer (CS Bio) with 2-Chlorotrityl Chloride resin as solid phase support following the instrument operation program. Details were described in the supplemental materials and methods.

Structural modeling with Rosetta FlexPepDock

The N-terminal structure of FOXM1 (PDB code 6OSW) was obtained from the Protein Data Bank database (PDB, <https://www.rcsb.org>). The structural model of peptide and FOXM1 was analyzed by Rosetta FlexPepDock [36], InterfaceAnalyzer [37], and Flex ddG [38]. Details were described in the supplemental materials and methods.

Microscale thermophoresis assay

Measurements were performed by Monolith NT.115 instrument (NanoTemper). The data were analyzed by MO. Affinity Analysis v2.3 NT software (NanoTemper) to determine interaction parameters. Details were described in the supplemental materials and methods.

Pull-down and co-immunoprecipitation (Co-IP) assays

Pull-down experiments were performed using Ni-Sepharose™ 6 Fast Flow (GE Healthcare, USA) and Streptavidin Agarose Resin (GE Healthcare, USA).

Co-IP experiment was performed using Flag magnetic beads (Bimake, USA). Details were described in the supplemental materials and methods.

Protein extraction and western blotting

The cells were lysed on ice with IP lysis buffer and tumor tissue samples were homogenized, grinded, and lysed on ice with RIPA buffer. The protein concentration of lysates was quantified using a BCA Protein Assay kit (Thermo Fisher Scientific, USA). Protein lysates were separated by SDS-PAGE gel electrophoresis and transferred to 0.22 μ m PVDF membranes (Merck Millipore, USA), followed by Western blotting with certain antibodies. Details were described in the supplemental materials and methods. Antibody information is available in Supplemental information Table S1. Uncropped immunoblot gels are shown in Original WB data.

RNA isolation and real-time quantitative PCR (RT-PCR)

TRIzol reagent (Invitrogen, USA) was used to extract the total RNA of cells according to the manufacturer's instructions. cDNA was synthesized from total RNA (2 μ g) by reverse transcription (Thermo Fisher Scientific, USA) according to the instructions provided by the manufacturer. RT-PCR was performed using SYBR QPCR Master Mix (Vazyme) with certain sense (S) and antisense (AS) primers, and realplex2 qPCR system (Eppendorf, Germany). The information on RT-PCR primer pairs was presented in Supplemental information Table S2.

RNA sequencing

MDA-MB-231 cells were treated with **M1-20** (10 μ m) or **M1-20mut** (10 μ m) for 24 h and collected into TRIzol reagent (Invitrogen, USA) and sent to Majorbio (Shanghai, China) for RNA extraction and sequencing. Details were described in the supplemental materials and methods.

The anti-cancer effects of M1-20 *in vivo*

Healthy ICR/JCL mice (6-week-old), BALB/c mice (female, 4-week-old), and BALB/c nude mice (female, 4-week-old) were purchased from Hunan Slac Laboratory Animal Company (Changsha, China). The detailed procedure was described in Supplementary Materials and Methods.

Ethics approval

All animal care and experiments were performed by the guidelines approved by the Laboratory Animal Center of Hunan, China (Protocol No. SYXK [Xiang] 2018-0006).

Statistical analysis

Data analysis and visualization were performed using Microsoft Excel and GraphPad Prism 9 (GraphPad Software Inc.). The analysis was tested by unpaired t-test between two groups, and by one-way ANOVA or two-way ANOVA with multiple comparisons in multiple groups. $P < 0.05$ was considered statistically significant.

RESULTS

FOXM1⁶⁸⁹⁻⁷⁴⁸ inhibited the transcriptional activities of FOXM1

Based on the FOXM1 C-terminal domain mediated by multiple PPIs, we constructed a series of expression vectors with the different length of FOXM1 C-terminus (pFOXM1₃₃₇₋₇₄₈, pFOXM1₅₈₀₋₇₄₈, and pFOXM1₆₈₉₋₇₄₈). We found that the over-expression of the each FOXM1 fragment inhibited the transactivation activity of FOXM1 to its luciferase reporter vector (p6xFOXM1Binding-Luc), in which FOXM1₆₈₉₋₇₄₈ showed the best inhibitory effect (Fig. 1A). FOXM1₁₋₆₈₈, in which the 689-748aa sequence was deleted from FOXM1, also lost transcriptional activity compared with full-length FOXM1 (Supplemental Fig. 1A). Co-immunoprecipitation (Co-IP) experiments showed that GFP-tagged FOXM1₆₈₉₋₇₄₈ interacted with exogenously expressed Flag-FOXM1 in cells (Fig. 1B) and in particular with FOXM1 N-terminus (His-FOXM1₁₋₁₃₈) (Fig. 1C). Recombinant protein GST-FOXM1₆₈₉₋₇₄₈ could pull down FOXM1 proteins from cell extracts (Supplemental Fig. 1B). We transfected HEK293T cells with expression vectors pGFP-FOXM1₆₈₉₋₇₄₈ and pRFP-FOXM1, and observed that they co-localized in the nucleus (Fig. 1D). We performed co-transfection

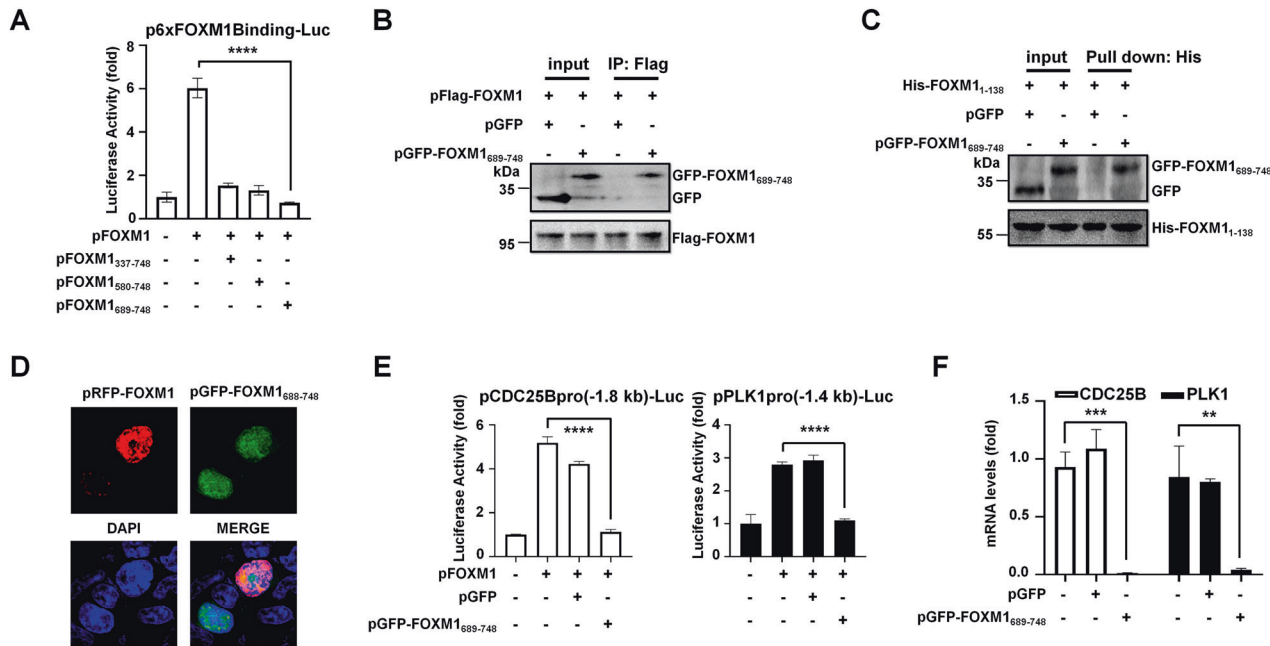


Fig. 1 FOXM1₆₈₉₋₇₄₈ inhibited the transcriptional activities of FOXM1. **A** The reporter plasmid, containing 6xFOXM1 binding sequences in its promoter (p6xFOXM1Binding-Luc, 1 μ g) were transfected with pFOXM1 (0.3 μ g) and different length of FOXM1 C-terminus (pFOXM1₃₃₇₋₇₄₈, pFOXM1₅₈₀₋₇₄₈, or pFOXM1₆₈₉₋₇₄₈, 0.3 μ g) into HEK293T cells, plus pRL-CMV plasmid (20 ng/well) as a loading control. After 48 h, cell lysates were collected and prepared for measurement of dual Luciferase activity. $n = 3$ for each group, **** $P < 0.0001$, two-tailed unpaired Student's t -test. **B** HEK293T cells were transfected with pFlag-FOXM1 and pGFP or pGFP-FOXM1₆₈₉₋₇₄₈ and 48 h later cell lysates were harvested. The lysates (500 μ g) were incubated with Flag magnetic beads to immunoprecipitate Flag-FOXM1/protein complexes which were analyzed by Western Blotting with certain antibodies. 10% of cell lysates (50 μ g) were used as input controls. **C** HEK293T cells were transfected with pGFP-FOXM1₆₈₉₋₇₄₈ or pGFP for 48 h. Purified protein His-FOXM1₁₋₁₃₈ added to His-tag resin were incubated with cell lysates (500 μ g) overnight at 4 $^{\circ}$ C. Pull-downs were analyzed by Western Blotting with Flag-tag and His-tag antibodies. 10% of cell lysates (50 μ g) were used as input controls. **D** HEK293T cells were transfected with pRFP-FOXM1 and pGFP-FOXM1₆₈₉₋₇₄₈ and 48 h later cells were fixed with 4% paraformaldehyde. The localization of GFP-FOXM1 and GFP-FOXM1₆₈₉₋₇₄₈ was imaged with the fluorescence confocal microscope (Olympus Fluoview FV1200). The DAPI signal indicated the location of the cell nucleus. **E** Reporter plasmids (1 μ g) containing the -1.8 kb CDC25B promoter-luciferase reporter (left) or the -1.4 kb PLK1 promoter-luciferase reporter (right) were transfected with pFOXM1 (0.3 μ g) and pGFP (0.3 μ g) or pGFP-FOXM1₆₈₉₋₇₄₈ (0.3 μ g) into HEK293T cells, plus pRL-CMV plasmid (20 ng/well) as a loading control. Cell lysates were prepared after 48 h and respectively used for the measurement of dual Luciferase activity. $n = 3$ for each group, **** $P < 0.0001$, two-tailed unpaired Student's t -test. **F** HEK293T cells were transfected with pGFP or pGFP-FOXM1₆₈₉₋₇₄₈ and 48 h later cells were collected for the preparation of total RNA. The mRNA levels of CDC25B and PLK1 were examined by RT-PCR. Relative mRNA levels were normalized to GAPDH. $n = 3$ for each group, ** $P < 0.01$, *** $P < 0.001$, two-tailed unpaired Student's t -test.

experiments and Luciferase assays to show that FOXM1 activated FKH-containing -1.8 kb CDC25B promoter [26] or CHR-containing -1.4 kb PLK1 promoter [28], while the expression of FOXM1₆₈₉₋₇₄₈ abolished the stimulation of FOXM1 on both promoters (Fig. 1E). The mRNA levels of CDC25B and PLK1 were also decreased in the FOXM1₆₈₉₋₇₄₈ expressed cells (Fig. 1F). Thus, the sequence 689-749aa of FOXM1 provided a potential natural amino acid sequence for screening FOXM1 interfering peptides.

The screening of the FOXM1-interacting peptide M1-20

We created a peptide library containing P1 to P9 peptides (20-mers, conjugated with TAT cell-penetrating sequence) with a moving window of five residues covering the sequence 689-748aa of FOXM1, for screening FOXM1-interacting peptides (Fig. 2A). Western blotting showed that P3, P5, P6, and P9 interacted with endogenous FOXM1 with variable affinities (Fig. 2A). Further investigation showed that only P5 (the sequence 709-728aa of FOXM1) (Supplemental Fig. 2A) significantly inhibited MDA-MB-231 breast cancer cells in a dose-dependent manner (Fig. 2B), providing a reason to focus on this peptide for further studies. Biotin-labeled P5 was found to bind to recombinant GST-FOXM1₁₋₁₃₈ protein but not GST control protein, confirming its ability to interact with FOXM1₁₋₁₃₈ (Fig. 2C). Rosetta FlexPepDock [36] was used to simulate a structure model for P5 binding to FOXM1₁₋₁₃₈ and Rosetta InterfaceAnalyzer [37] was performed to

calculate the docking free energy (the value of dG around -49 kcal/mol) for the interface between P5 and FOXM1₁₋₁₃₈ (Fig. 2D). Single point mutation with alanine scanning by Rosetta Flex ddG [38] revealed that the three residues in P5 (L721, I723, and S724 of FOXM1) were predicted as the core sites for mediating P5 interaction with FOXM1₁₋₁₃₈ (Fig. 2D). Mutating the three residues in P5 to obtain P5mut (L721A, I723A, S724A) (Supplemental Fig. 2B) led to loss of FOXM1₁₋₁₃₈ binding ability (the value of free energy change $\Delta\Delta G > 1$ kcal/mol) (Fig. 2D). Microscale Thermophoresis was performed to measure the binding affinity of P5 to FOXM1₁₋₁₃₈ with $K_D = 43.1$ μ M, while the binding of P5mut to FOXM1₁₋₁₃₈ was unmeasurable (Fig. 2E). Next, we adopted the D-retro-inverso (DRI) strategy, in which DRI peptides were composed of D-amino acid assembled in the reverse order of natural parent peptides [39], to optimize the stability of P5. We synthesized the DRI form of P5 to obtain M1-20 (Supplemental Fig. 3A), which maintained a similar secondary structure as the parent P5 measured by Circular Dichroism (Supplemental Fig. 4). Compared with P5, M1-20 showed much better resistance to degradation in HEK293T cell lysates (Fig. 2F), and a stronger inhibitory ability to MDA-MB-231 cells (Fig. 2G). Pull-down results showed that FOXM1₁₋₁₃₈ was bound by M1-20 but not M1-20mut (Fig. 2H, Supplemental Fig. 3B). Microscale Thermophoresis further confirmed the binding ability of M1-20 to FOXM1₁₋₁₃₈ with $K_D = 5.658$ μ M, much stronger than that of M1-20mut

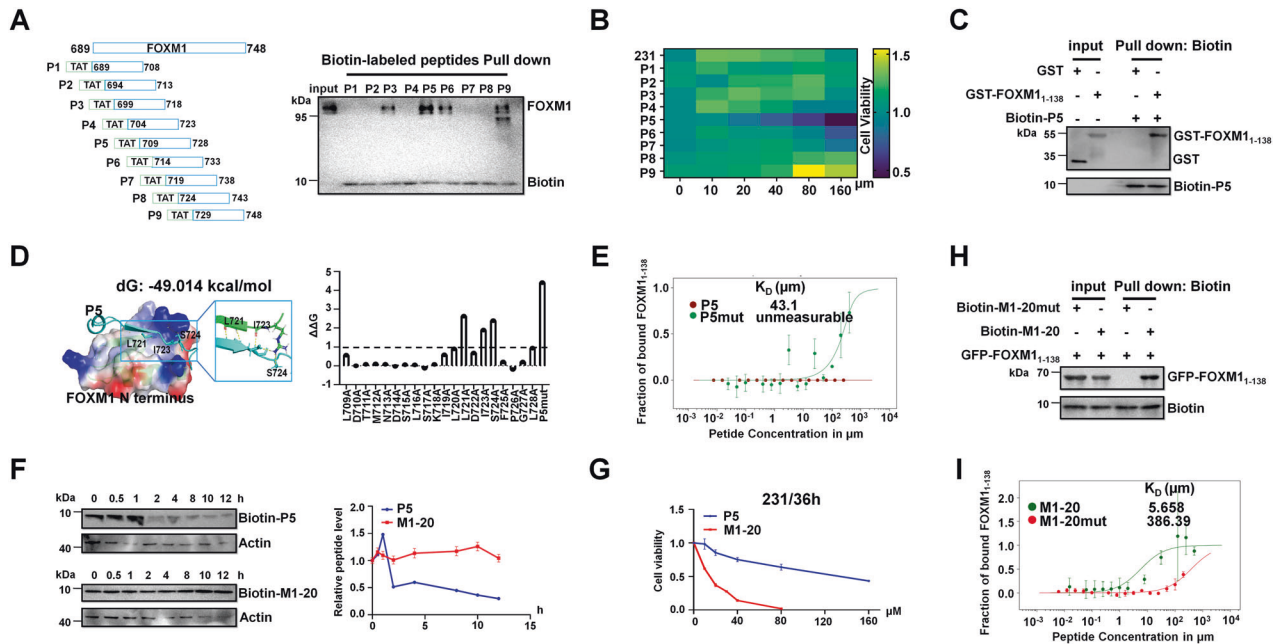


Fig. 2 The screening of the FOXM1-interacting peptide M1-20. **A** The diagram of peptide array (P1–P9) in which peptides (20-mer) covering FOXM1_{689–748} with a shifting window of five residues were conjugated to the cell-penetrating peptide TAT and produced by solid-phase peptide synthesis. The P1–P9 peptides were biotin-labeled respectively and added in MDA-MB-231 cell lysates (500 μ g) which were incubated with Streptavidin Agarose Resin to pull down biotin-peptide/protein complexes. Biotin and FOXM1 proteins in samples were detected by Western Blotting with certain antibodies. 10% of cell lysates (50 μ g) were used as input controls. **B** MDA-MB-231 cells (4×10^3 cells/well) were seeded in 96-well plates for 12 h and treated with a defined concentration gradient of the P1–P9 peptides (0, 10, 20, 40, 80, 160 μ M). 36 h later, CCK-8 solution (10%) was added to each well and incubated for another 2 h. The absorbance at 450 nm and the relative cell viability in each well was calculated. The percentage of cell activity versus the concentration of peptides was plotted by heatmap. $n = 3$ for each group. **C** Recombinant protein GST-FOXM1_{1–138} (50 μ g) was added to biotin-labeled P5 (10 μ g) which was incubated with Streptavidin Agarose Resin to pull down biotin-peptide/protein complexes. GST protein was used as a control. GST-tag and Biotin-tag were detected by Western Blotting with certain antibodies. 10% of recombinant protein was used as input controls. **D** The model of P5 binding to the N-terminus of FOXM1 (PDB ID 6OSW) was built by Rosetta FlexPepDock. Left, the interface of peptide-protein interaction, the peptide was shown in cyan, and the N-terminus of FOXM1 was shown as electrostatic potential in Protein. Right, hydrogen bonds were formed by core residues at the interface of peptide and protein interaction. The curve was shown the free energy change ($\Delta\Delta G$) by single point mutation with alanine scanning using Rosetta Flex ddG ($\Delta\Delta G \geq 1$, binding energy decreases; $1 > \Delta\Delta G > -1$, binding energy no changes; $\Delta\Delta G \leq -1$, binding energy increases). **E** The curve represents the quantification of binding affinity between GFP-labeled FOXM1_{1–138} and P5 or P5mut by Microscale Thermophoresis (MST, Monolith NT.115, NanoTemper). Data points indicated the fraction of FOXM1_{1–138}-bound peptide (Δ Normal/Amplitude) at different concentrations, and curves indicated the calculated fits. Error bars represent the SE of three independent measurements. Mean values of binding affinity were shown on the panel. **F** The biotin signals indicated the peptide stability of P5 and M1-20 in HEK293T cell lysates analyzed by Western Blotting. The levels of peptide were quantified by Image J software and graphed with GraphPad Prism 9 ($n = 3$). **G** MDA-MB-231 cells were seeded in 96-well plates for 12 h and treated with different concentrations of P5 or M1-20. 36 h later CCK-8 solution (10%) was added to each well and incubated for another 2 h. The absorbance at 450 nm and the relative cell viability in each well was calculated and plotted by GraphPad Prism 9. $n = 3$ for each group. **H** Recombinant protein His-FOXM1_{1–138} (50 μ g) added to biotin-labeled M1-20 (10 μ g) or M1-20mut (10 μ g) was incubated with Streptavidin Agarose Resin to pull down biotin-peptide/protein complexes. GFP-tag and Biotin-tag in samples were detected by Western Blotting with certain antibodies. 10% of the recombinant protein/peptide complex was used as input controls. **I** Quantification of binding affinity between GFP-labeled FOXM1_{1–138} and M1-20 or M1-20mut by Microscale Thermophoresis. Mean values of binding affinity were shown on the panel. Experiments were repeated three times with similar results.

($K_D = 386.39 \mu\text{M}$) or parent P5 ($K_D = 43.1 \mu\text{M}$) (Fig. 2I and see above).

M1-20 suppressed multiple types of cancer cells and affected multiple cancer cell phenotypes

We selected multiple types of cancer cell lines and treated with M1-20 by a defined concentration gradient (0, 10, 20, 40, 60, 80 μ M) for 36 h. Compared with M1-20mut, M1-20 significantly inhibited all of cancer cells in a dose-dependent manner (Fig. 3). The values of IC₅₀ of M1-20 were calculated for each cell line (18.15 μ M for MBA-MD-231, 31.05 μ M for MCF-7, 23.57 μ M for ZR-75-30, 42.95 μ M for HeLa, 25.65 μ M for U2OS, 32.47 μ M for A549), showing variable sensitivities for different cancer cells responding to the M1-20 treatment. Interestingly, we also noticed that M1-20 resulted in no or mild inhibition of normal cell lines at the tested dosages (Fig. 3C), implicating relative safety for M1-20 use in vivo. In the meantime, we demonstrated that cells with higher FOXM1

protein levels exhibited greater sensitivity to M1-20 treatment while displaying lower IC₅₀ values of M1-20 (Supplemental Fig. 5A). In addition, the overexpression of FOXM1 in MCF7 or HeLa cells with relatively low endogenous levels of FOXM1 resulted in heightened sensitivity towards M1-20 (Supplemental Fig. 5B, C), supporting that M1-20's anti-cancer efficacy correlated with the FOXM1 levels in cancer cells.

Next, we focused on MDA-MB-231 cells for analyzing the effects of M1-20 on the cellular processes of cancer cells. From the RNA-seq data of M1-20 or M1-20mut-treated MDA-MB-231 cells (10 μ M for 24 h), we noticed that multiple signaling pathways were significantly changed based on the gene set enrichment analysis (GSEA) using differentially expressed genes (DEGs) (Supplemental Fig. 6A). The gene sets of cell cycle (E2F targets) were suppressed in M1-20-treated cells (Fig. 4A), predicting that the proliferation of the cells was affected by M1-20. We found that the mRNA levels of Ki-67 and the mRNA and protein of PCNA were

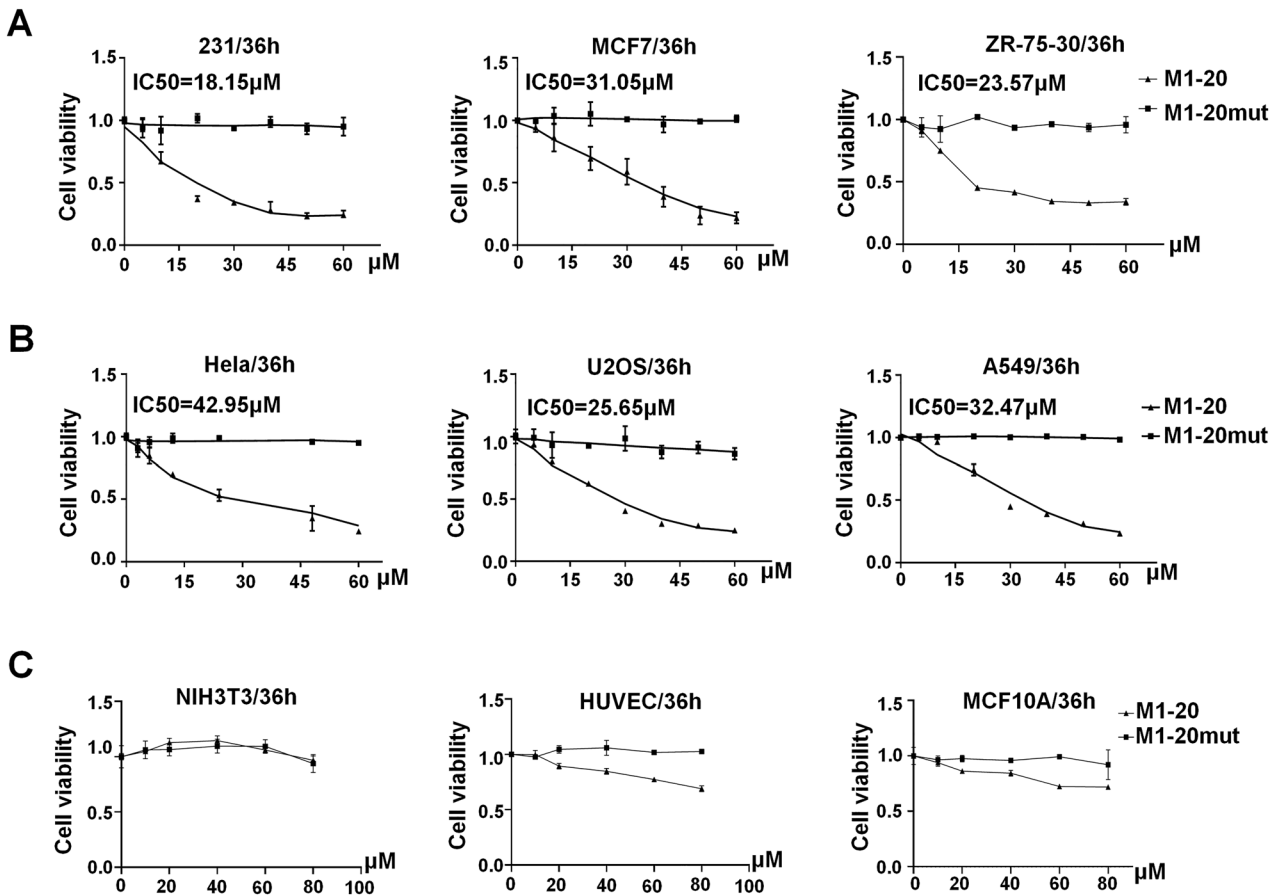


Fig. 3 **M1-20 suppressed the growth of cancer cells.** **A** Cell viability of breast cancer cells (MDA-MB-231, MCF7, ZR-75-30 cells) after incubation with different **M1-20** concentrations for 36 h. **B** Cell viability of various cancer cells (Hela, U2OS, A549 cells) after treatment of **M1-20** for 36 h. **C** Cell viability of normal cells (NIH3T3, HUVEC, MCF10A cells) after treatment of **M1-20** for 36 h. Cells (4×10^3 cells/well) were seeded in 96-well plates for 12 h and treated with a defined concentration gradient of **M1-20** or **M1-20mut** (5, 10, 20, 30, 40, 50, 60, 80 μM). 36 h later CCK-8 solution (10%) was added to each well and incubated for another 2 h. The absorbance at 450 nm and the relative cell viability in each well was calculated. The percentage of cell activity versus the concentration of **M1-20** was plotted ($n = 3$ for each group). The IC₅₀ value of **M1-20** for each cell line was calculated with GraphPad Prism 9.

downregulated by **M1-20** (10 μM for 24 h) in MDA-MB-231 cells (Fig. 4B, C), correlated with the decreased proliferation of the cells in EdU staining experiments (Fig. 4D, Supplemental Fig. 6B). This finding was further supported by flow cytometry analysis, in which **M1-20** reduced S-phase fraction and increased G1-phase fraction in the cells (Supplemental Fig. 6C), correlated with the decreased levels of CyclinD1, CyclinB1, and PLK1 (Supplemental Fig. 6D). The gene set of cell adhesion was activated by **M1-20** (Fig. 4E). The mRNA levels and protein levels of the epithelial marker E-cadherin enhancing cell adhesion were elevated and the levels of the mesenchymal marker Vimentin abolishing cell adhesion were declined by **M1-20** (Fig. 4F, G), correlated with the decreased migration of the cells in Wound Healing assays (Fig. 4H, Supplemental Fig. 5E). In addition, the gene set of apoptosis was activated by **M1-20** (Fig. 4I). The mRNA levels and protein levels of Bax and Caspase 3 were upregulated by **M1-20** (10 μM for 24 h) in MDA-MB-231 cells (Fig. 4J, K). Consequently, elevated levels of sub-G1 apoptotic bodies (Supplemental Fig. 6C), TUNEL staining (Fig. 4L, Supplemental Fig. 6F), and Annexin-positive apoptotic cells (Supplemental Fig. 6G) were observed in MDA-MB-231 cells treated with **M1-20**. **M1-20** inhibited the colony formation of MDA-MB-231 cells (Fig. 4M). To further test whether **M1-20** suppressed the progression of cancers in vivo, we made mouse cancer-engrafted models by subcutaneously implanting MDA-MB-231 cells (1×10^7 cells/mouse) into BALB/c nude mice. We found that treatment with **M1-20** resulted in dramatic cancer

suppression (Fig. 4N, O), consistent with the changed levels of the marker proteins specific for proliferation and apoptosis in the collected cancer tissues post **M1-20** treatment (Fig. 4P). Furthermore, we noticed that the protein levels of cancer stem cell markers ALDH1 and CD44 were also decreased in the **M1-20**-treated cancer tissues (Supplemental Fig. 6H), implicating that the population of cancer stem cells in the grafted cancers were altered by the **M1-20** treatment.

M1-20 inhibited FOXM1-related transcriptional activities

Although it was detected in both cytoplasm and nucleus, **M1-20** majorly localized in the nucleus of cells (Fig. 5A). Interestingly, **M1-20** also affected the distribution of FOXM1 in cells, resulting in the elevated levels of FOXM1 in cytoplasm and the declined levels of FOXM1 in nucleus (Fig. 5A). Electrophoretic Mobility Shift Assays (EMSA) showed that **M1-20** did bind to FOXM1 but not disrupt its DNA binding ability (Fig. 5B). Because **M1-20** bound to FOXM1 N-terminus that interacted with the MuvB complex [27], we asked whether **M1-20** affected the interaction between FOXM1 and the key component of the MuvB complex, LIN9, which recruited FOXM1 and bound to CHR-containing promoters, such as the promoter of PLK1 [28]. We performed Co-IP experiments to verify that the interaction of FOXM1:LIN9 was disrupted in cells by **M1-20** in a dose-dependent manner (Fig. 5C). This was further supported by co-transfection experiments, in which **M1-20** abolished the FOXM1-MuvB-mediated stimulation on the

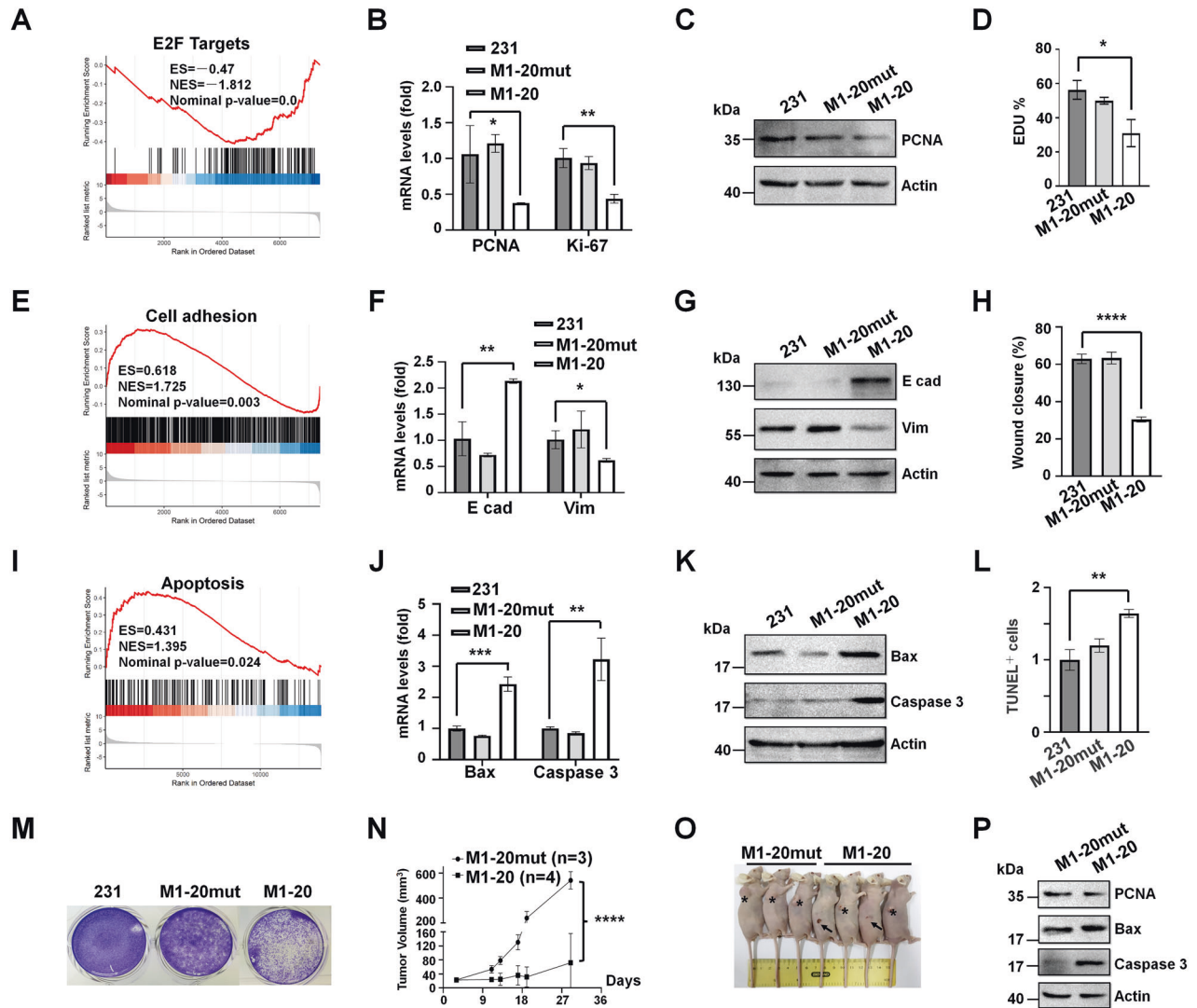


Fig. 4 M1-20 inhibited the proliferation and migration of cancer cells, and induced the apoptosis of cancer cells. **A** MDA-MB-231 cells were treated with M1-20 (10 μ M) or M1-20mut (10 μ M) and 24 h later the cells were collected in Trizol to extract the total RNA for RNA sequencing. The gene set of cell cycle (E2F targets) was significantly downregulated by M1-20 in gene set enrichment analysis (GSEA) using differentially expressed genes (DEGs). **B**, **C** MDA-MB-231 cells were treated with M1-20 (10 μ M) or M1-20mut (10 μ M) and 24 h later the cells were collected for the preparation of total RNA (**B**) and total proteins (**C**). The mRNA levels of PCNA and Ki-67 were examined by RT-RCR. Relative mRNA levels were normalized to GAPDH. $n = 3$ for each group. * $P \leq 0.05$, ** $P < 0.01$, *** $P < 0.001$, two-tailed unpaired Student's t-test. Protein levels were measured by Western blotting with certain antibodies. **D** MDA-MB-231 cells were treated with M1-20 (10 μ M) for the detection of cell proliferation with EdU. Mean fluorescence intensity of EdU was measured by Image J ($n = 3$, * $P < 0.05$). **E** The gene set of cell adhesion was significantly upregulated by M1-20 in GSEA analysis. **F**, **G** MDA-MB-231 cells were treated as (**B**), (**C**). The mRNA levels (**F**) and protein levels (**G**) of E-cadherin (E cad) and Vimentin (Vim) were respectively examined by RT-PCR and Western blotting. **H** MDA-MB-231 cells were treated with M1-20 (10 μ M) for the detection of cell migration by wound-healing assay. The cell migration area was calculated by Image J ($n = 3$, **** $P \leq 0.0001$). **I** The gene set of apoptosis was significantly upregulated by M1-20 in GSEA analysis. **J**, **K** MDA-MB-231 cells were treated as (**B**), (**C**). The mRNA levels (**J**) of Bax and Caspase 3 were examined by RT-PCR. Protein levels (**K**) were measured by Western blotting with certain antibodies. **L** MDA-MB-231 cells were treated with M1-20 (10 μ M) and detected apoptosis by TUNEL. TUNEL-positive cell content was quantified between the groups ($n = 3$, ** $P \leq 0.01$). **M** MDA-MB-231 cells (400 cells/well) were seeded in 6-well plates and treated with M1-20 (10 μ M) or M1-20mut (10 μ M) for 14 days. The cells were fixed with 4% paraformaldehyde, stained with 0.1% crystal violet, and imaged. **N** The nude mice (female, 4–6 weeks old) were subcutaneously (S.C.) injected with MDA-MB-231 cells (1×10^7 cells/mouse). When the tumor volume reached about 20 mm³, the mice were randomized into two groups (at least three mice per group) and orthotopically injected with M1-20mut (4 mg/kg) or M1-20 (4 mg/kg). The volume of tumors was measured twice weekly using electronic and growth curves were obtained on Day 29. Tumor volume (V) was calculated by: $V = \text{length} \times \text{diameter}^2 \times 1/2$. Significant differences were shown, 2-way ANOVA (Sidak's multiple-comparisons test): **** $P \leq 0.0001$. **O** At the end of the experiment, mice were imaged. Tumor localization in mice was marked with asterisks and tumor disappearance in two mice of the M1-20 group was indicated by arrows. **P** The protein levels of PCNA, Bax, and Caspase 3 in collected tumor tissues were measured by western blotting.

–1.4 kb PLK1 promoter (Fig. 5D), similar to the effects of the LIN9 siRNA treatment (Supplemental Fig. 7). In addition, because the transcriptional activation of FOXM1 on FKH-containing promoters relied on recruiting transcriptional co-activator CBP at FOXM1

C-terminus [40], we verified that M1-20 disrupted the interaction between FOXM1 and CBP by Co-IP experiments (Fig. 5E). M1-20 abolished the FOXM1-mediated stimulation on the FKH-containing promoters in co-transfection experiments (Fig. 5F).

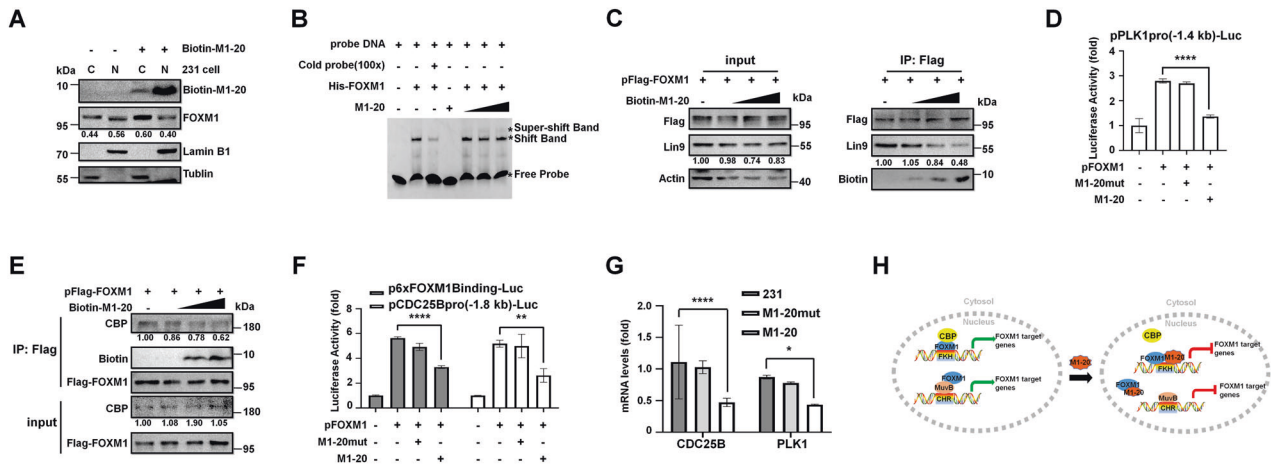


Fig. 5 **M1-20 inhibited FOXM1-related transcriptional activities.** **A** MDA-MB-231 cells were seeded in 6 cm plates for 12 h and then treated with **M1-20** (10 μ M) containing 10% biotin-labeled **M1-20**. After treatment for 24 h, the cells were harvested for the separation of the cytoplasmic and nuclear proteins. The levels of **M1-20** in the cytoplasm (C) or the nucleus (N) were analyzed by Western blotting. α -Tubulin or Lamin B1 was used as a cytoplasmic or nuclear marker, respectively. **B** The EMSA experiment was performed by recombinant His-FOXM1 proteins (2 μ M) and the FAM-labeled DNA probe (50 nM). **M1-20** was added to the reactions with increasing concentrations (5 μ M and 10 μ M). The Cold probe (100 \times , 5 mM) was unlabeled with FAM to show the specificity of FOXM1/DNA complex formation. The reactions were performed in 4% native polyacrylamide gel electrophoresis in 0.5 \times TBE buffer and imaged with Kodak 4000 MM Imaging System (EX: 465 nm, EM: 535 nm for FAM). **C** HeLa cells were transfected with pFlag-FOXM1 (6 μ g) for 48 h. Cell lysates were harvested and respectively incubated with Flag magnetic beads, added to different dosages of biotin-labeled **M1-20** (0 μ g, 2 μ g, 4 μ g, 8 μ g). Flag-FOXM1/protein complexes were analyzed by Western Blotting with certain antibodies. 10% of cell lysates (50 μ g) were used as input controls. The levels of protein were quantified by Image J software. **D** The -1.4 kb PLK1 promoter-luciferase reporter plasmid (1 μ g) and pRL-CMV plasmid (20 ng/well) were co-transfected with pFOXM1 (0.3 μ g) into HeLa cells. 12 h later **M1-20** (20 μ M), and **M1-20mut** (20 μ M) were respectively added to the selected transfections. Then cell lysates were prepared 24 h later and used for the measurement of dual Luciferase activities. $n = 3$ for each group, **** $P < 0.0001$, two-tailed unpaired Student's t-test. **E** HEK293T cells were transfected with pFlag-FOXM1 (6 μ g) and 48 h later the cells were collected. The cell lysates (500 μ g) were incubated with Flag magnetic beads and added with different quality of **M1-20** (0 μ g, 2 μ g, 4 μ g, 8 μ g) to immunoprecipitation Flag-FOXM1/protein complexes. CBP, Biotin, and Flag proteins in samples were detected by Western Blotting with certain antibodies. 10% of cell lysates (50 μ g) were used as input controls. **F** Reporter plasmids containing the 6 \times FOXM1 binding sequence (1 μ g) or the -1.8 kb CDC25B promoter-luciferase reporter (1 μ g) were co-transfected with pFOXM1 (0.3 μ g) into HEK293T cells, plus pRL-CMV plasmid (20 ng/well) as a loading control. 12 h later **M1-20** (20 μ M) or **M1-20mut** (20 μ M) was added to the selected transfections. Another incubation for 24 h later cell lysates were prepared for the measurement of dual Luciferase activities. $n = 3$ for each group, ** $P < 0.01$, two-tailed unpaired Student's t-test. **G** MDA-MB-231 cells were treated with **M1-20** (10 μ M) or **M1-20mut** (10 μ M) and 24 h later the cells were collected for the preparation of total RNA. The mRNA levels of CDC25B and PLK1 were examined by RT-PCR. $n = 3$ for each group, **** $P \leq 0.0001$, two-tailed unpaired Student's t-test. **H** The diagram depicting the molecular mechanisms of **M1-20** inhibiting the FOXM1-related transcriptional activities.

Finally, we measured the mRNA levels of FOXM1 typical target genes, CDC25B and PLK1, and observed the downregulated levels of both genes in MDA-MB-231 cells post **M1-20** treatment (10 μ M for 24 h) (Fig. 5G), further supporting the molecular mechanisms summarized in a diagram (Fig. 5H) for **M1-20** inhibiting FOXM1-related transcriptional activities.

M1-20 inhibited the progression of cancers in wild-type mice

Next, mouse cancer models with wild-type backgrounds and intact immune systems were used to analyze **M1-20** anti-cancer effects in vivo. Both domains of human FOXM1 (1-138aa and 689-748aa) were highly conserved with those of mouse Foxm1 (Supplemental Fig. 8A). Biotin-labeled **M1-20** could bind to endogenous Foxm1 from mouse breast cancer 4T1 cell lysates (Supplemental Fig. 8B) and as expected, **M1-20** inhibited 4T1 cells at a dose-dependent manner (Supplemental Fig. 8C). 4T1 cells (1×10^6 cells/injection) were subcutaneously implanted in the left and right flanks of wild-type BALB/c mice (Fig. 6A). Compared with the PBS and **M1-20mut** groups, the intraperitoneal injection of **M1-20** resulted in the inhibition of cancer growth (Fig. 6B), and significantly reduced the size and weight of engrafted cancers (Fig. 6C), corresponding to the decreased levels of proliferation-related CDC25B, PLK1, PCNA, and increased levels of apoptosis-related Bax and Caspase 3 in **M1-20**-treated cancer samples (Supplemental Fig. 9A, B). Immunostaining showed that the levels of PCNA were downregulated and the levels of Caspase 3 were upregulated post the **M1-20** treatment (Supplemental Fig. 9C).

Our results demonstrated that systemic administration of **M1-20** exhibited a strong anti-cancer effect in wild-type animals.

To investigate the impact of **M1-20** on the metastasis of cancer cells in wild-type mice, we constructed a stable luciferase-GFP-expressed cell line with 4T1 cells (4T1-Luc-GFP) (Supplemental Fig. 10). 4T1-Luc-GFP cells (5×10^5 cells/mouse) were injected into BALB/c mice (females, 4–6 weeks of age) via tail-vein (Fig. 6D). Therapeutic efficacy was monitored by bioluminescence imaging, which was performed by randomly selecting three mice with the intraperitoneal injection of D-Luciferin potassium salt (3 mg/200 μ L/mouse) at different time points after **M1-20** systemic administration (Day 7 and Day 11). Bioluminescent signals showed that **M1-20** prevented the metastasis of cancer cells in a dose-dependent manner (Fig. 6E). One mouse was randomly taken from each group on Day 8 to analyze metastatic cancer cells in different organs. Lumina imaging and H&E staining revealed that **M1-20** inhibited the metastasis of cancer cells mainly to the lung (Fig. 6F, G). The expression levels of migration-related genes in metastatic cancer cells of lung tissue were also altered by **M1-20** treatment (Supplemental Fig. 11). The survival of animals was monitored throughout the experiments, with the survival curve illustrating that **M1-20** significantly prolonged survival time in a dose-dependent manner (Fig. 6H). These results demonstrated that systemic administration of **M1-20** showed a potent anti-metastasis effect on cancer cells and improved the survival of animals.

To evaluate the safety of **M1-20**, H&E staining on tissue sections from BALB/c mice treated with **M1-20** showed no obvious

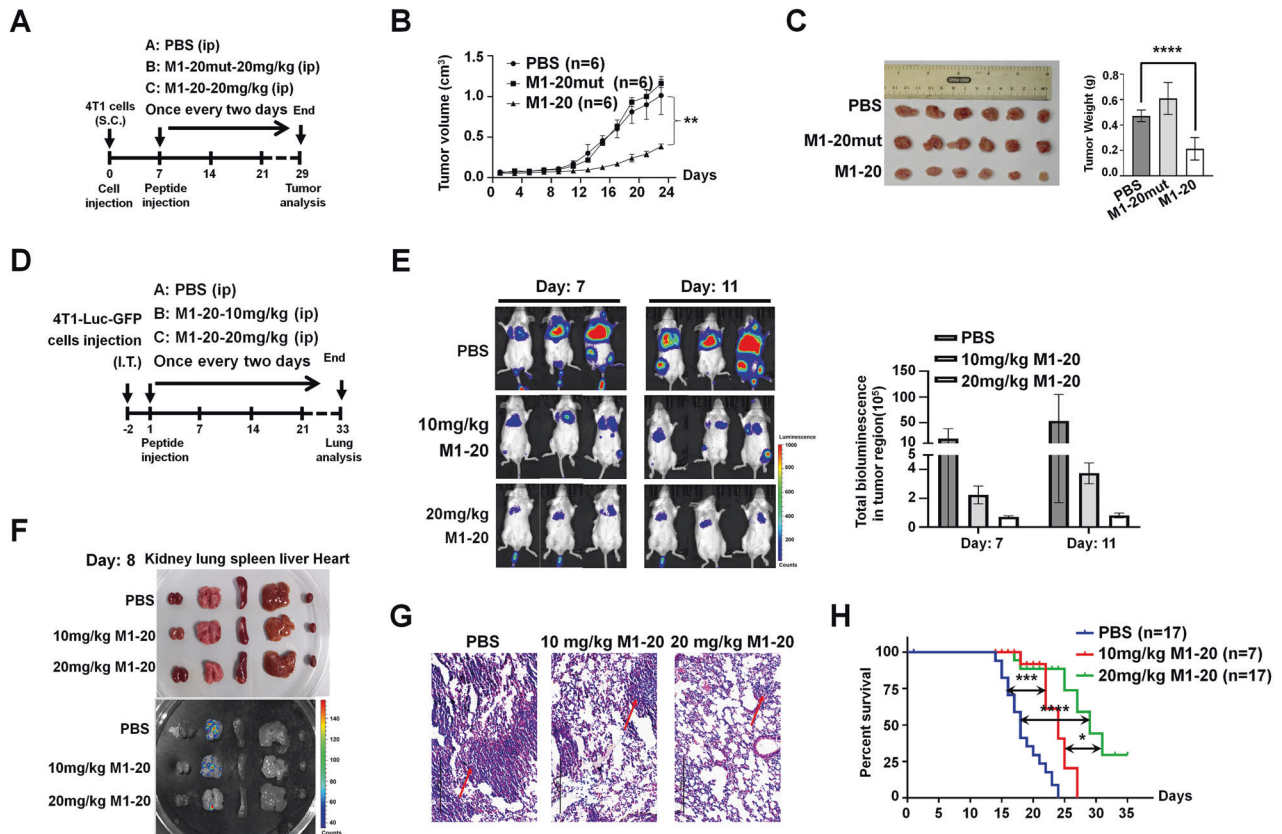


Fig. 6 **M1-20 inhibited the progression of cancers in wild-type mice.** **A** BALB/c mice (female, 4–6 weeks old) were subcutaneously (S.C.) injected with 4T1 cells (1×10^6 cells/injection) into the left and right flank. One week later, the mice were randomly divided into three groups (three mice/group) and intraperitoneally (I.P.) injected with PBS, **M1-20mut** (20 mg/kg) or **M1-20** (20 mg/kg) for three weeks. **B** Tumor volume was measured every two days and growth curves were obtained at the end of the experiment. Tumor volume (V) was calculated as: $V = \text{length} \times \text{diameter}^2 \times 1/2$. Significant differences were shown, 2-way ANOVA (Sidak's multiple-comparisons test): $**P \leq 0.01$. **C** The images and weight of engrafted tumors at the end of the experiment ($****P \leq 0.0001$). **D** BALB/c mice (female, 4–6 weeks old) were injected intravenously with 4T1-Luc-GFP cells (5×10^4 cells/mouse). After three days, the mice were randomized into three groups and injected (I.P.) with PBS, **M1-20** (10 mg/kg, 20 mg/kg) every two days. **E** The growth of metastatic 4T1-Luc-GFP cancer cells was observed on Day 7 and Day 11 with the intraperitoneal injection of D-Luciferin potassium salt (3 mg/200 μL /mouse) through whole-body bioluminescence imaging by IVIS Lumina XR. Fluorescence intensities in three mice selected randomly were measured by the Living Image[®] software. **F** Ex vivo fluorescence images of different organs on Day 8 after **M1-20** treatment were taken using IVIS Lumina XR. **G** The status of metastatic lung cancer tissue on Day 8 was performed by H&E staining. Representative images were shown. Scale bar: 20 μm . **H** Survival statistics for the mice were graphed using GraphPad Prism 9 software with Mantel-Cox estimator and log-rank test ($*P \leq 0.05$, $**P \leq 0.01$, $***P \leq 0.001$, $****P \leq 0.0001$).

morphological lesions in multiple organs (Supplemental Fig. 12A). Hemolysis analysis demonstrated that **M1-20** with a concentration gradient (25, 50, 100, 200, 400, 800 $\mu\text{g}/\text{ml}$) incubated with blood cells did not induce obvious hemolysis (Supplemental Fig. 12B). Acute toxicity test results showed that wild type ICR/JCL mice [41, 42] could tolerate doses of **M1-20** up to 200 mg/kg body weight by intraperitoneal injection with no observed toxicity (Supplemental Fig. 12C). ELISA assays showed no significant increase in the generation of **M1-20**-specific antibodies at the time points tested compared with pre-**M1-20** injection (Supplemental Fig. 12D). Together, these results showed that **M1-20** was well-tolerated and safe at its dose of anti-cancer therapy in vivo.

DISCUSSION

Peptides have many favorable characteristics, such as moderate molecular weight, high binding affinities, significant target specificities, and relatively safe and well-tolerated, which have garnered much attention for the development of anti-cancer drugs [3]. In particular, interfering peptides possess advantages for disrupting transcription factor-involved PPIs due to the large and flat contact surfaces. In this study, we have developed a novel FOXM1-interfering peptide **M1-20** that potently represses FOXM1

functions by disrupting PPIs between FOXM1 and its multiple partner proteins.

M1-20 binds to the N-terminal domain of FOXM1 with relatively high affinity ($K_D = 5.658 \mu\text{M}$) to disrupt the interaction between FOXM1 and the MuvB complex, thereby inhibiting FOXM1 transcriptional activities on certain cell cycle genes such as PLK1. Furthermore, we have noted that **M1-20** can abolish the interaction between FOXM1 and CBP without affecting FOXM1's DNA-binding ability, explaining the inhibition of FOXM1 direct downstream genes such as CDC25B. In addition, FOXM1 activity is induced by the phosphorylation of multiple sites in its C-terminal domain by cell cycle-related protein kinases during mitosis, such as CDK1 [30] and PLK1 [40], which are essential protein kinases in G2/M phase to stimulate cell cycle progression and are considered as therapeutic targets in various cancers [43]. Interestingly, both kinases appear on the list of **M1-20**-interacting candidates from our ongoing Mass Spectrometry Analysis with high confidence (data not shown). Therefore, it is worth testing whether **M1-20** acts as an inhibitor for both kinases in future studies.

Generally, natural peptides (composed of natural L-amino acids) are highly susceptible to protease degradation, resulting in poor stability and limited therapeutic potential [39]. The development of DRI peptides, which incorporate D-amino acids as stable surrogates

of L-amino acids but are assembled in a reverse (retro) order compared with the parent peptide [44], provides an efficient approach to overcome these limitations. Since their side chains adopt a topology similar to that of the parent peptide [45], DRI peptides have the potential to achieve the same functions as their parent L-peptides with superior stability towards proteolytic degradation [44]. Several DRI peptides have been evaluated as anti-tumor drug candidates in preclinical studies, e.g., DRI peptide RE-A7R targeting VEGFR2 [46], FOXO4-DRI peptide targeting p53:FOXO4 interaction [47], or in clinical trials, e.g., AM111 targeting JNK:c-Jun interaction [48]. In this study, **M1-20**, the DRI form of the **P5** peptide, possesses a prolonged half-life in cell lysates and exhibits a conformation similar to **P5**. The binding affinity and inhibitory potency of **M1-20** to cancer cells are dramatically improved, indicating the successful optimization of the peptide using the DRI strategy. In addition, many other approaches have been proposed to optimize peptides, including amino acid substitution, cyclization, side chain stapling, PEGylation, or lipidation [49], which can be explored for the selected **P5** peptide in the future.

Although **M1-20** has been primarily studied for its anti-tumor effects in breast cancer models, it has the potential to inhibit various types of cancer by targeting the FOXM1 protein. The levels of FOXM1 are elevated in almost all clinical cancer types from the TCGA database [50]. Conditional knockout of FOXM1 inhibits cancer development in multiple mouse organs, such as the liver [51], lung [52], and rectum [53]. Our studies have also demonstrated that adenovirus-mediated interference with FOXM1 expression impedes the progression of liver cancer [54], breast cancer [13], and nasopharyngeal carcinoma [55]. While **M1-20** has been shown to inhibit various cancer cell lines in cell culture, its effects on different solid tumors in vivo require further investigation. Furthermore, **M1-20** may have potential benefits in cancer treatment when combined with standard chemotherapy or radiotherapy. Recently, studies have demonstrated the involvement of FOXM1 in chemoresistance [12], and several FOXM1-targeting small molecule compounds, such as Siomycin A plus 5-FU [22], Thiostrépton plus Selumetinib [56], and FDI-6 plus PARP inhibitor Olaparib [57], have been tested in combination therapy to overcome drug resistance in cancer treatment. These combinations have been explored as a solution to the narrow clinical indications and adaptive resistance of FOXM1 inhibitors. As peptides display minimal susceptibility to drug resistance [58], it is possible that combining **M1-20** with standard chemoradiotherapy could improve the efficacy of cancer treatment.

This study focuses on the therapeutic targeting of FOXM1 with **M1-20**, with the aim of altering cancer cell phenotypes such as proliferation, migration, and apoptosis. Notably, treatment with **M1-20** leads to down-regulation of cancer stem cell markers including ALDH1 and CD44 (Supplemental Fig. 6H), suggesting its potential in modulating cancer stem cell populations. Given that FOXM1 plays a crucial role in maintaining cancer stem cell properties [15], further studies should explore the effects of **M1-20** on cancer stem cell populations during initial and recurring stages of cancer. Such evidence could inform optimal therapeutic timing of **M1-20** in clinical settings. Overall, our study provides valuable insights into the therapeutic effects of **M1-20** against cancers and suggests that it may be a promising candidate for further clinical investigation.

DATA AVAILABILITY

All data generated or analyzed during this study are included in this manuscript and its Supplementary Information files. Additional data are available from the corresponding author upon reasonable request.

REFERENCES

- Bushweller JH. Targeting transcription factors in cancer - from undruggable to reality. *Nat Rev Cancer*. 2019;19:611–24.
- Lambert M, Jambon S, Depauw S, David-Cordonnier MH. Targeting transcription factors for cancer treatment. *Molecules*. 2018;23:1479.
- Bruzzoni-Giovanelli H, Alezra V, Wolff N, Dong CZ, Tuffery P, Rebollo A. Interfering peptides targeting protein-protein interactions: the next generation of drugs? *Drug Discov Today*. 2018;23:272–85.
- Wang X, Ni D, Liu Y, Lu S. Rational design of peptide-based inhibitors disrupting protein-protein interactions. *Front Chem*. 2021;9:682675.
- Schneider JA, Craven TW, Kasper AC, Yun C, Haugbro M, Briggs EM, et al. Design of peptoid-peptide macrocycles to inhibit the beta-catenin TCF interaction in prostate cancer. *Nat Commun*. 2018;9:4396.
- Di Agostino S, Cortese G, Monti O, Dell'Orso S, Sacchi A, Eisenstein M, et al. The disruption of the protein complex mutantp53/p73 increases selectively the response of tumor cells to anticancer drugs. *Cell Cycle*. 2008;7:3440–7.
- Zhai D, Chin K, Wang M, Liu F. Disruption of the nuclear p53-GAPDH complex protects against ischemia-induced neuronal damage. *Mol Brain*. 2014;7:20.
- Warso MA, Richards JM, Mehta D, Christov K, Schaeffer C, Bressler LR, et al. A first-in-class, first-in-human, phase I trial of p28, a non-HDM2-mediated peptide inhibitor of p53 ubiquitination in patients with advanced solid tumours. *Brit J Cancer*. 2013;108:1061–70.
- Soucek L, Helmer-Citterich M, Sacco A, Jucker R, Cesareni G, Nasi S. Design and properties of a Myc derivative that efficiently homodimerizes. *Oncogene*. 1998;17:2463–72.
- Hannenhalli S, Kaestner KH. The evolution of Fox genes and their role in development and disease. *Nat Rev Genet*. 2009;10:233–40.
- Kalin TV, Ustiyani V, Kalinichenko VV. Multiple faces of FoxM1 transcription factor. Lessons from transgenic mouse models. *Cell Cycle*. 2011;10:396–405.
- Koo CY, Muir KW, Lam EW. FOXM1: from cancer initiation to progression and treatment. *Biochim Biophys Acta*. 2012;1819:28–37.
- Yang C, Chen H, Yu L, Shan L, Xie L, Hu J, et al. Inhibition of FOXM1 transcription factor suppresses cell proliferation and tumor growth of breast cancer. *Cancer Gene Ther*. 2013;20:117–24.
- Yang C, Chen H, Tan GX, Gao W, Cheng L, Jiang X, et al. FOXM1 promotes the epithelial to mesenchymal transition by stimulating the transcription of Slug in human breast cancer. *Cancer Letters*. 2013;340:104–12.
- He C, Jaffar Ali D, Qi Y, Li Y, Sun B, Liu R, et al. Engineered extracellular vesicles mediated CRISPR-induced deficiency of IQGAP1/FOXM1 reverses sorafenib resistance in HCC by suppressing cancer stem cells. *J Nanobiotechnology*. 2023;21:154.
- Tan Y, Raychaudhuri P, Costa RH. Chk2 mediates stabilization of the FoxM1 transcription factor to stimulate expression of DNA repair genes. *Mol Cell Biol*. 2007;27:1007–16.
- Zhang N, Wu X, Yang L, Xiao F, Zhang H, Zhou A, et al. FoxM1 inhibition sensitizes resistant glioblastoma cells to temozolomide by downregulating the expression of DNA-repair gene Rad51. *Clin Cancer Res*. 2012;18:5961–71.
- Nestal de Moraes G, Delbue D, Silva KL, Robaina MC, Khongkow P, Gomes AR, et al. FOXM1 targets XIAP and Survivin to modulate breast cancer survival and chemoresistance. *Cell Signal*. 2015;27:2496–505.
- Borhani S, Gartel AL. FOXM1: a potential therapeutic target in human solid cancers. *Expert Opin Ther Targets*. 2020;24:205–17.
- Hegde NS, Sanders DA, Rodriguez R, Balasubramanian S. The transcription factor FOXM1 is a cellular target of the natural product thiostrépton. *Nat Chem*. 2011;3:725–31.
- Shukla S, Milewski D, Pradhan A, Rama N, Rice K, Le T, et al. The FOXM1 inhibitor RCM-1 decreases carcinogenesis and nuclear beta-catenin. *Mol Cancer Ther*. 2019;18:1217–29.
- Klinhom-On N, Seubwai W, Sawanyawisuth K, Obchoei S, Mahalapbutr P, Wongkham S. FOXM1 inhibitor, Siomycin A, synergizes and restores 5-FU cytotoxicity in human cholangiocarcinoma cell lines via targeting thymidylate synthase. *Life Sci*. 2021;286:120072.
- Ulhaka K, Kanokwiroon K, Khongkow M, Bissanum R, Khunpitak T, Khongkow P. The anticancer effects of FDI-6, a FOXM1 inhibitor, on triple negative breast cancer. *Int J Mol Sci*. 2021;22:6685.
- Xiang Q, Tan G, Jiang X, Wu K, Tan W, Tan Y. Suppression of FOXM1 transcriptional activities via a single-stranded DNA aptamer generated by SELEX. *Sci Rep*. 2017;7:45377.
- Zhang Z, Bu H, Yu J, Chen Y, Pei C, Yu L, et al. The cell-penetrating FOXM1 N-terminus (M1-138) demonstrates potent inhibitory effects on cancer cells by targeting FOXM1 and FOXM1-interacting factor SMAD3. *Theranostics*. 2019;9:2882–96.
- Littler DR, Alvarez-Fernandez M, Stein A, Hibbert RG, Heidebrecht T, Aloy P, et al. Structure of the FoxM1 DNA-recognition domain bound to a promoter sequence. *Nucleic Acids Res*. 2010;38:4527–38.
- Sadasivam S, Duan S, DeCaprio JA. The MuvB complex sequentially recruits B-Myb and FoxM1 to promote mitotic gene expression. *Genes Dev*. 2012;26:474–89.

28. Muller GA, Wintsche A, Stangner K, Prohaska SJ, Stadler PF, Engeland K. The CHR site: definition and genome-wide identification of a cell cycle transcriptional element. *Nucleic Acids Res.* 2014;42:10331–50.
29. Chen X, Muller GA, Quaa M, Fischer M, Han N, Stutchbury B, et al. The forkhead transcription factor FOXM1 controls cell cycle-dependent gene expression through an atypical chromatin binding mechanism. *Mol Cell Biol.* 2013;33:227–36.
30. Major ML, Lepe R, Costa RH. Forkhead box M1B transcriptional activity requires binding of Cdk-cyclin complexes for phosphorylation-dependent recruitment of p300/CBP coactivators. *Mol Cell Biol.* 2004;24:2649–61.
31. Das C, Roy S, Namjoshi S, Malarkey CS, Jones DN, Kutateladze TG, et al. Binding of the histone chaperone ASF1 to the CBP bromodomain promotes histone acetylation. *Proc Natl Acad Sci USA.* 2014;111:E1072–81.
32. Boija A, Mahat DB, Zare A, Holmqvist PH, Philip P, Meyers DJ, et al. CBP regulates recruitment and release of promoter-proximal RNA polymerase II. *Mol Cell.* 2017;68:491–503.e5.
33. Zhang N, Wei P, Gong A, Chiu WT, Lee HT, Colman H, et al. FoxM1 promotes beta-catenin nuclear localization and controls Wnt target-gene expression and glioma tumorigenesis. *Cancer Cell.* 2011;20:427–42.
34. Xue J, Lin X, Chiu WT, Chen YH, Yu G, Liu M, et al. Sustained activation of SMAD3/SMAD4 by FOXM1 promotes TGF-beta-dependent cancer metastasis. *J Clin Invest.* 2014;124:564–79.
35. Marceau AH, Brison CM, Nerli S, Arsenault HE, McShan AC, Chen E, et al. An order-to-disorder structural switch activates the FoxM1 transcription factor. *Elife.* 2019;8:e46131.
36. Raveh B, London N, Schueler-Furman O. Sub-angstrom modeling of complexes between flexible peptides and globular proteins. *Proteins.* 2010;78:2029–40.
37. Stranges PB, Kuhlman B. A comparison of successful and failed protein interface designs highlights the challenges of designing buried hydrogen bonds. *Protein Sci.* 2013;22:74–82.
38. Barlow KA, Ó Conchúir S, Thompson S, Suresh P, Lucas JE, Heinonen M, et al. Flex ddG: Rosetta ensemble-based estimation of changes in protein-protein binding affinity upon mutation. *J Phys Chem B.* 2018;122:5389–99.
39. Doti N, Mardirossian M, Sandomenico A, Ruvo M, Caporale A. Recent applications of retro-inverso peptides. *Int J Mol Sci.* 2021;22:8677.
40. Fu Z, Malureanu L, Huang J, Wang W, Li H, van Deursen JM, et al. Plk1-dependent phosphorylation of FoxM1 regulates a transcriptional programme required for mitotic progression. *Nat Cell Biol.* 2008;10:1076–82.
41. Nomura T. Comparison of tumour susceptibility among various organs of foetal, young and adult ICR/Jcl mice. *Br J Cancer.* 1976;33:521–34.
42. Sher SP. Tumors in control mice: literature tabulation. *Toxicol Appl Pharmacol.* 1974;30:337–59.
43. Linton A, Cheng YY, Griggs K, Schedlich L, Kirschner MB, Gattani S, et al. An RNAi-based screen reveals PLK1, CDK1 and NDC80 as potential therapeutic targets in malignant pleural mesothelioma. *Br J Cancer.* 2018;118:e13.
44. Xi W, Hansmann UHE. The effect of retro-inverse D-amino acid Abeta-peptides on Abeta-fibril formation. *J Chem Phys.* 2019;150:095101.
45. Garton M, Nim S, Stone TA, Wang KE, Deber CM, Kim PM. Method to generate highly stable D-amino acid analogs of bioactive helical peptides using a mirror image of the entire PDB. *Proc Natl Acad Sci USA.* 2018;115:1505–10.
46. Ying M, Zhan C, Wang S, Yao B, Hu X, Song X, et al. Liposome-based systemic glioma-targeted drug delivery enabled by all-d peptides. *ACS Appl Mater Interf.* 2016;8:29977–85.
47. Baar MP, Brandt RMC, Putavet DA, Klein JDD, Derks KWJ, Bourgeois BRM, et al. Targeted apoptosis of senescent cells restores tissue homeostasis in response to chemotoxicity and aging. *Cell.* 2017;169:132.
48. Chiquet C, Aptel F, Creuzot-Garcher C, Berrod JP, Kodjikian L, Massin P, et al. Postoperative ocular inflammation: a single subconjunctival injection of XG-102 compared to dexamethasone drops in a randomized trial. *Am J Ophthalmol.* 2017;174:76–84.
49. Corbi-Verge C, Garton M, Nim S, Kim PM. Strategies to develop inhibitors of motif-mediated protein-protein interactions as drug leads. *Annu Rev Pharmacol Toxicol.* 2017;57:39–60.
50. Liao GB, Li XZ, Zeng S, Liu C, Yang SM, Yang L, et al. Regulation of the master regulator FOXM1 in cancer. *Cell Commun Signal.* 2018;16:57.
51. Park HJ, Gusarova G, Wang ZB, Carr JR, Li J, Kim KH, et al. Deregulation of FoxM1b leads to tumour metastasis. *Embo Mol Med.* 2011;3:21–34.
52. Wang IC, Ustiyani V, Zhang Y, Cai Y, Kalin TV, Kalinichenko VV. Foxm1 transcription factor is required for the initiation of lung tumorigenesis by oncogenic Kras(G12D). *Oncogene.* 2014;33:5391–6.
53. Yoshida Y, Wang IC, Yoder HM, Davidson NO, Costa RH. The forkhead box M1 transcription factor contributes to the development and growth of mouse colorectal cancer. *Gastroenterology.* 2007;132:1420–31.
54. Chen T, Xiong J, Yang C, Shan L, Tan G, Yu L, et al. Silencing of FOXM1 transcription factor expression by adenovirus-mediated RNA interference inhibits human hepatocellular carcinoma growth. *Cancer Gene Ther.* 2014;21:133–8.
55. Chen H, Yang C, Yu L, Xie L, Hu J, Zeng L, et al. Adenovirus-mediated RNA interference targeting FOXM1 transcription factor suppresses cell proliferation and tumor growth of nasopharyngeal carcinoma. *J Gene Med.* 2012;14:231–40.
56. Demirtas Korkmaz F, Dogan Turacli I, Esendagli G, Ekmekci A. Effects of thios-trepton alone or in combination with selumetinib on triple-negative breast cancer metastasis. *Mol Biol Rep.* 2022;49:10387–97.
57. Wang SP, Wu SQ, Huang SH, Tang YX, Meng LQ, Liu F, et al. FDI-6 inhibits the expression and function of FOXM1 to sensitize BRCA-proficient triple-negative breast cancer cells to Olaparib by regulating cell cycle progression and DNA damage repair. *Cell Death Dis.* 2021;12:1138.
58. Shao N, Yuan L, Ma P, Zhou M, Xiao X, Cong Z, et al. Heterochiral beta-peptide polymers combating multidrug-resistant cancers effectively without inducing drug resistance. *J Am Chem Soc.* 2022;144:7283–94.

ACKNOWLEDGEMENTS

This study was supported by grants from the National Natural Science Foundation of China (No. 81773169, No. 81472718), Hunan Key R&D Project (2023SK2040), China Changsha Development and Reform Commission “Mass entrepreneurship and innovation program” (2018-68) and “Innovation platform construction program” (2018-216).

AUTHOR CONTRIBUTIONS

YT conceived the study. HB and XL performed the experiments and analyzed the data. HC, CP, and MO contributed to data acquisition or analysis. HB, XL, HC, and CP were involved in experimental design and data analysis. YT, LY, and XH provided technical or material support. YT, HB, and XL wrote and edited the manuscript. YT, LY, XH, and YC supervised the project, and YT performed project administration and funding acquisition.

COMPETING INTERESTS

A patent on **M1-20** and its derivatives has been granted in China (ZL202011200439.0). YT and HB are co-inventors of this patent. This does not alter the authors’ adherence to the policies on sharing data and materials.

ADDITIONAL INFORMATION

Supplementary information The online version contains supplementary material available at <https://doi.org/10.1038/s41419-023-06056-9>.

Correspondence and requests for materials should be addressed to Yongjun Tan.

Reprints and permission information is available at <http://www.nature.com/reprints>

Publisher’s note Springer Nature remains neutral with regard to jurisdictional claims in published maps and institutional affiliations.



Open Access This article is licensed under a Creative Commons Attribution 4.0 International License, which permits use, sharing, adaptation, distribution and reproduction in any medium or format, as long as you give appropriate credit to the original author(s) and the source, provide a link to the Creative Commons license, and indicate if changes were made. The images or other third party material in this article are included in the article’s Creative Commons license, unless indicated otherwise in a credit line to the material. If material is not included in the article’s Creative Commons license and your intended use is not permitted by statutory regulation or exceeds the permitted use, you will need to obtain permission directly from the copyright holder. To view a copy of this license, visit <http://creativecommons.org/licenses/by/4.0/>.

© The Author(s) 2023